Characterization of a Dipole Surface Drive Actuator With Large Travel and Force

Manu Agarwal, *Member, IEEE*, David T. Dutton, Jeremy A. Theil, *Senior Member, IEEE*, Qing Bai, Evelyn Par, and Storrs Hoen, *Member, IEEE*

***Abstract*—This paper presents a detailed study of the dynamic performance of an electrostatic surface drive actuator. This actuator is capable of producing 50 g's of acceleration with 70 μm travel at a 30 V bias. For the first time, air operation of a dipole surface actuator is demonstrated and we describe a fabrication process that has increased device yield more than an order of magnitude. Detailed characterization of the actuator performance is enabled by the integration of a capacitive position sensor that provides 0.5 Å resolution in a 1-Hz bandwidth. The performance of this actuator is compared with other micromachined actuators and with more conventional milliactuators. [1736]**

***Index Terms*—2-D actuator, actuator, air operation, capacitive sensing, dipole, electrostatic, electrostatic snap-in, fringing field forces, microactuator, micromachining, micromover, nanopositioner, position sensing, surface actuator, surface drive.**

I. Introduction

MILLIMETER-SCALE actuators are ubiquitous in consumer products. These "milliactuators" drive the hands of our watches, position the lenses in our CD and DVD players, and move the relay arms present in many electronic devices. It is important to ask why micromachined actuators have not reached the same presence in the consumer market. In general, the micromachined actuators with the largest market reach, such as accelerometers [1] and Texas Instruments digital light processing (DLP) arrays [2], move themselves rather than external objects. This paper represents a step toward designing micromachined actuators that can be used to position and accelerate lenses, gratings, mirrors, and other external objects. Examples of possible applications are miniature tunable lasers [3], low-cost portable imaging systems for scanning probe microscopes [4]–[6], optical data storage applications [7], and actuators for tilting mirrors [8], [9]. The fabrication of large travel actuators is a rich area of research. Most of the published actuators rely on electrostatic forces; examples are comb drives [10], gap-closing actuators [11], scratch drive actuators [12], bending beam actuators [13], and side electrode actuators for mirrors [14]. There has also been considerable work on magnetic actuation methods, such as induction [15], voice coil [6], [16], and stepping motors [17]. Alternative technologies such as pneumatics [18] and shape memory alloys [19], [20] have also been studied.

Most notably, Grade *et al.* have produced a single axis electrostatic comb drive that traverses 150–200 μm in less than 1 ms at a bias of less than 150 V [21], [22]. Rodgers *et al.* have developed a compact comb drive that generates 1.5 $\mathrm{mN/mm^2}$ at 100 V with a range of motion of several microns [10]. These actuators provide excellent performance; however, significant progress is still required to replace milliactuators with micromachined actuators.

We previously reported a high-performance dipole surface drive actuator with large travel and rapid acceleration [23], [24]. The previous fabrication process had an extremely low yield of $\sim$1% primarily because of the fine line geometry necessary for the translator and stator electrodes. In this paper, we describe a process that has increased the device yield to 50% and allowed the actuator to operate in air.

Many applications require precise and rapid positioning. Micromachined actuators often have very little damping if their geometry does not induce squeeze film damping; thus making them susceptible to overshoot and ringing. While fluid encapsulants can be used to mitigate this problem, [21], [25] they make packaging and handling more difficult. Active feedback can provide the advantages of rapid positioning but it requires a sensor integrated with the actuator. Fortunately, the two-plate geometry of the dipole surface drive is ideally suited to capacitive sensing techniques. Hartwell *et al.* [26] have described a fine line capacitive sensor integrated with a dipole surface drive. While sensitive, their sensor does not provide an unambiguous position output. In contrast, the large plate sensors described in this paper provide one-to-one mapping between the actuator position and the sensor output. These sensors are used to provide the most detailed characterization to date of the dynamics of a dipole surface drive. Available force and acceleration are studied as functions of the bias voltage, actuator position, and voltage pattern applied to the stator electrodes. Snap-in between the translator and stator is studied in detail and, for the first time, air operation of a dipole surface drive is described.

II. Basic Principles of Operation

In this section, we describe the basic principles of operation. A scanning electron micrograph (SEM) of the top view of a one-dimensional (1-D) actuator is shown in Fig. 1(a). The flat translator stage measures 2.5 $\times$ 2.1 mm and is suspended above the stator by folded beam flexures. Because the top of the translator is featureless, it is ideally suited for mounting mirrors, gratings, lenses and other external components. The driving force applied to the translator arises from fringing fields created on the interior surfaces of the translator and stator. To create these fields for an x-actuator, long strip electrodes oriented along the y-direction are formed on the translator as shown in Fig. 1(b). Similarly oriented electrodes are formed along the stator surface. A full description of the motor fabrication is provided in the discussion of Fig. 3.

Manuscript received January 1, 2006; revised June 12, 2006. Subject Editor R. R. A. Syms.

The authors are with Agilent Laboratories, Palo Alto, CA 94304 USA (e-mail: amanu@stanford.edu).

Color version of Fig. 3 available online at http://ieeexplore.ieee.org.

Digital Object Identifier 10.1109/JMEMS.2006.883886

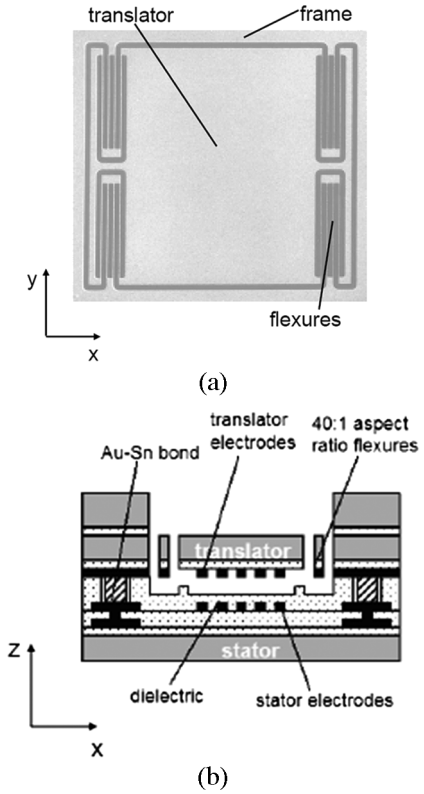

Fig. 1. (a) SEM of the top of the translator stage. (b) Schematic cross-section of the dipole stepper motor.

Detailed electrostatic formalism has been discussed previously for a two-dimensional (2-D) surface drive actuator [23], [27]. The 1-D actuator that we discuss here is a simpler version, with electrodes aligned only along the y-direction and no corresponding flexures for y-translation. The lateral force F_x applied to the translator depends on the gap d between the translator and stator, the voltages applied to both sets of electrodes and the pitch p_t of the translator electrodes. In general, it should be expressed as a summation over a series of spatial Fourier components. However, the behavior is dominated by a single term in the summation. For this term, the spatial wavevector $k = \pi/p_t$ and F_x can be expressed as follows:

$$F_x \cong \frac{\varepsilon_0 k^2 V_b^2}{4} \left(\frac{2 J_s J_t \sin(k x_0)}{\sinh(kd)} \right) \tag{1}$$

where ε_0 is the permittivity of free space and x_0 is the displacement of the translator origin relative to the stator origin in the x-direction [27]. Here, J_s and J_t are the components of the spatial Fourier transforms at the wavevector k of the stator and translator voltage patterns respectively. Both J_s an J_t have been normalized to the applied bias voltage V_b. Similarly, we can express the out-of-plane force F_z between the translator and stator as follows:

$$F_z \cong F_{z0} + \frac{\varepsilon_0 k^2 V_b^2}{4} \left[\frac{-\left(J_s^2 + J_t^2\right)}{\sinh^2(kd)} + \frac{2 J_s J_t \cos(k x_0) \cosh(kd)}{\sinh^2(kd)} \right] \tag{2}$$

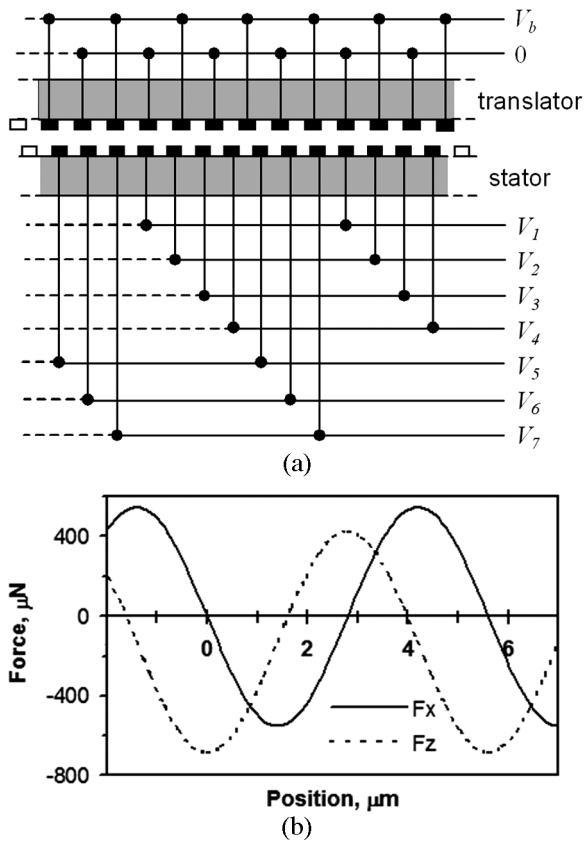

Fig. 2. (a) Schematic wiring diagram of the translator and stator electrodes. The translator electrodes alternate between $\mathrm{V_b}$ and ground while a seven phase voltage pattern described in Table I is applied to the stator electrodes. (b) Lateral force ($\mathrm{F_x}$) and out-of-plane force ($\mathrm{F_z}$) calculated as functions of translator position for a bias voltage of 40 V, a gap of 2.4 μm, an actuator area of 1.84 $\mathrm{mm^2}$ and a translator pitch of 2.8 μm.

where

$$F_{z0} = \left(-\varepsilon_0 V_b^2 / 2d^2\right) \left(J_{s0} + J_{t0}\right) \tag{3}$$

and $J_{s0}$and J_{t0} are the spatial averages of the voltage patterns applied to the surfaces of the stator and translator, respectively, both normalized to the applied bias voltage [27].

We configure the electrodes on the bottom of the translator so that every other electrode is at the bias voltage while alternate electrodes are held at ground. This dipole voltage pattern is shown in Fig. 2(a). The stator electrodes are arranged so that each electrode is electrically connected to the electrode seven electrodes away. Moreover, the stator pitch is chosen so that for every six translator electrodes there are seven stator electrodes. For the particular actuators described in this paper, the translator electrode pitch p_t and the stator electrode pitch p_s are 2.8 and 2.4 μm, respectively.

A voltage pattern such as Pattern A in Table I is applied to the stator electrodes so that a basically spatially alternating voltage pattern is generated on its surface. The interaction of the two spatially alternating patterns on the translator and stator surfaces causes the translator to sit in the sinusoidal force field as depicted in Fig. 2(b). The period of the sinusoidal force curve is equal to $2p_t$, the period of the dipole voltage pattern on the translator. In the absence of external forces, the translator rests where the force curve crosses zero with negative slope as that is a stable equilibrium position.

TABLE I
VOLTAGE PATTERNS APPLIED TO THE ELECTRODES SHOWN IN FIG. 2(A)

	Stator Electrode Voltage						
	V_1	V_2	V_3	V_4	V_5	V_6	V_7
Pattern A	0	V_b	0	V_b	V_b	0	V_b
Pattern B	0	V_b	0	0	V_b	0	V_b
Pattern C	0	V_b	V_b	0	V_b	0	V_b
Pattern D	0	$0.9V_b$	V_b	0	V_b	0	V_b

To move the translator, the voltage on one stator electrode is changed from V_b to ground or *visa versa*. Table I shows an example of this method in which Pattern A is changed to Pattern B and then to Pattern C by changing the voltage on one electrode at a time. This causes the electrical potential to be shifted in steps of $p_t/7$ or 0.4 μm. The translator rest position is similarly shifted by 0.4 μm. The voltages applied to the *translator* electrodes are not altered when the actuator is moved. This is important because the lead connecting the translator electrodes to the external bias must be routed along the underside of the folded beam flexures. For the TiN electrodes used in this process, there is a 5 kΩ resistive drop along the flexures. If the bias were not held relatively constant on the translator, there would be significant heat generated along the flexures. To move the actuator in increments of less than the 400 nm basic step size, we change the voltage on one electrode by a fraction of V_b [27].

III. METHOD OF FABRICATION

In our prior work [23], the fabrication process suffered from extremely low yields of $\sim$1%. Much of the yield loss arose from the fine line geometry of the translator and stator electrodes. While 1.2 μm lines and spaces are large by current CMOS standards, they are difficult to fabricate in a conventional micromachining facility. In addition, the prior process required a vapor HF etch and the handling and bonding of extremely fragile wafers. The two-wafer process described in Fig. 3 solves each of these problems and has increased our device yield to $\sim$50%.

The initial processing of the stator and translator wafers occurs in a conventional CMOS foundry. The stator wafer is fabricated on a standard wafer with a first level aluminum metallization followed by an interlayer dielectric that is capped with an ammonia-free silicon nitride. Interlayer tungsten plugs connect the aluminum with an upper layer metallization of TiN that is patterned to form the stator electrodes. The complete structure is then capped with a 2.5 μm oxide overlayer. The TiN metallization and ammonia-free silicon nitride were selected in order to allow wet etching of the oxide overlayer. The wafer, as returned from the CMOS fab, is shown in Fig. 3(a). Two wet field oxide etches then create the bumpers and stand offs as shown in Fig. 3(b). The standoffs determine the gap between the translator and stator while the bumpers ensure that the electrodes do not contact each other when the translator snaps down toward the stator. Conformal layers of sputtered 500 Å AlN and 500 Å PECVD oxide are deposited as shown in (3b). The AlN appears to reduce the shielding by mobile ions during air operation and serves as an etch stop for fluorine-based plasma etches used later in the process. Openings are patterned in this dielectric stack to provide electrical contact between the stator and translator. A 200 Å chrome adhesion layer is deposited followed by a 2000 Å Au seed layer for plating. The structure is then plated with 2.5 μm Au followed by 1 μm Sn. After seed layer removal, the wafer appears as shown in Fig. 3(c).

The translator wafer is initially processed in a CMOS foundry using silicon-on-insulator (SOI) wafers as starting material. The 100 μm thick "translator" layer is supported by a 380 μm thick "handle" layer with a 0.5-μm-thick buried oxide. The translator uses a single layer TiN metallization that is patterned to form the translator electrodes. A thin protective oxide is deposited to protect the electrodes during subsequent processing. As returned from the CMOS foundry, the wafer appears as shown in Fig. 3(d). A 4-μm-thick PECVD oxide is first deposited on the backside of the wafer and a Cr protective layer is deposited on the front side. The thick oxide is patterned with a dry etch to provide a deep-silicon etch mask at the end of the process. The protective Cr layer is stripped immediately after the plasma etch and the oxide is removed from several places over the TiN metallization. A 250 Å Cr layer followed by a 2000 Å Au layer are deposited and patterned around these openings to provide electrical contact between the translator and stator. This is followed by a two-step flexure etch, a standard BOSCH process deep reactive-ion etch (DRIE) followed by a stop-on-oxide plasma etch. The wafer now appears as shown in Fig. 3(e).

The translator is then attached to the stator at 320°C using an aligned wafer bond as shown in Fig. 3(f). At this stage the wafer stack is robust and can be handled with standard processing tools. The process is completed by removing the portion of the 400 μm handle wafer from the backside of the translator with a deep silicon etch followed by a dry oxide etch. The AlN deposited on the stator protects the TiN electrodes and underlying insulator during this etch. The fully released actuator appears as shown in Fig. 3(g).

IV. SENSOR CHARACTERIZATION

Many applications require a position sensor integrated with the actuator. As mentioned previously, the small 2.5 μm gap between the translator and stator allow the construction of a very sensitive capacitive position detector. In a prior article [26], a periodic array of fine pitched sensor electrodes was used to detect the actuator position. While such an array has excellent sensitivity, it does not provide unambiguous mapping between the translator position and the sensor output voltage.

In contrast, the present design uses large plate electrodes shown schematically in the top left inset of Fig. 4 so that the sensor output increases monotonically with actuator position. As shown in the inset of Fig. 4, four 200 μm wide $\times$ 96 μm long plate electrodes are fabricated on the translator with 100 μm pitch along the x-direction. These dimensions allow sensing of the full 70 μm travel and accommodate any misalignment that occurs during fabrication. A companion set of five similarly sized electrodes is fabricated on the stator. These sensor electrodes, while fabricated on the same surfaces as the actuator

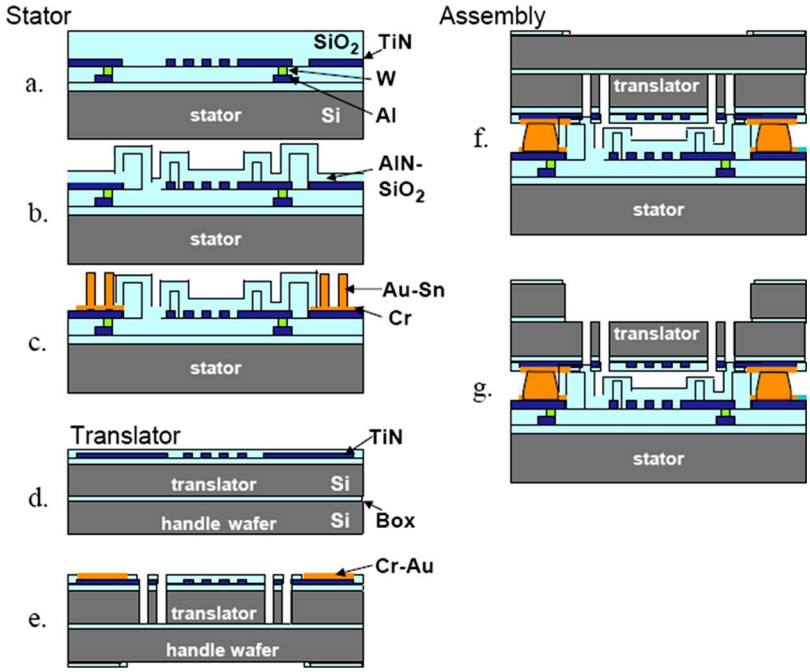

Fig. 3. Fabrication process for the actuator. (a)–(c) Stator process flow. (d) and (e) Translator process flow. (f) and (g) Wafer bonding and post-wafer bonding process for the actuator.

electrodes, have a much different geometry than the actuator electrodes that typically have dimensions of 1.2 μm wide by 1-mm long.

Two 5 V_{rms} 250 kHz sinusoidal signals are applied to the translator electrodes with the voltages on adjacent electrodes being 180° out-of-phase. The actuator position is synchronously detected by monitoring the phase and amplitude of the signals coupled into the stator plates. The signals from alternate stator sense plates are connected to a differential buffer amplifier comprised of two OPA 656 FET-input operational amplifiers. The primary noise source arises from the interaction between the buffer amplifier and the high impedance of the sensor. These amplifiers were chosen for their low 2.8 pF input capacitance and their low current and voltage noise, 1.3 fA and 7 nV, respectively, in 1 Hz bandwidths. The resulting buffered signal is then mixed with a phase-shifted version of the drive signal to produce the output signal. The resolution was measured to be 0.5 Å in a 1 Hz bandwidth.

Fig. 4 shows the sensor output voltage plotted as a function of actuator position and bias voltage applied to the translator and stator electrodes. The sensor remains linear over the entire range of motion for each bias voltage. The null output of the sensor occurs when the actuator is offset from the origin by 10 μm, corresponding to the measured misalignment from the bonding process. As the voltage is increased, the translator moves closer to the stator along the z-axis and more 250 kHz signal is coupled into the stator electrodes. Hence, an increase in responsivity is observed, as shown in the bottom right inset of Fig. 4.

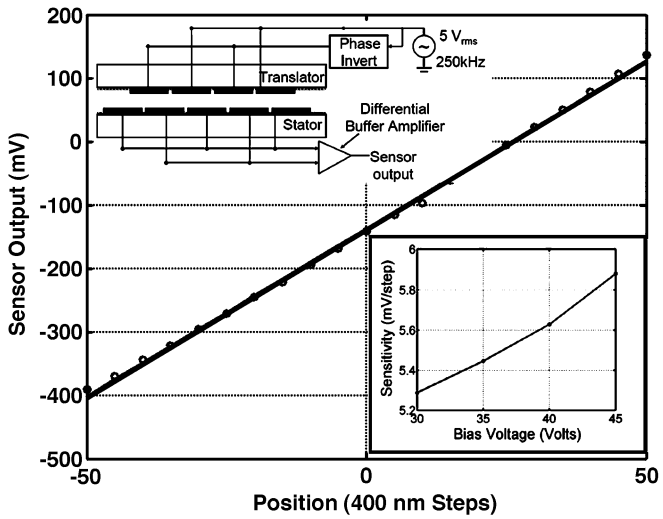

Fig. 4. Sensor output voltage is plotted against the translator position with a bias voltage of 30 V. The inset plot (top left) shows the sensor schematic. The other inset plot (bottom right) shows the sensitivity w.r.t. the bias voltage. Each step corresponds to changing the voltage applied to one electrode from V_b to ground or *vice versa*. Such a flip moves the stator voltage profile by 400 nm.

V. Actuator Performance

Each actuator application has a large and varied set of performance requirements. The available force and travel are often the most important of these requirements, though resonant frequency, operating voltage, reliability, precision, size, cost, and efficiency are also likely to play key roles. In this section, we present measurements on the actuator acceleration and resonant frequency as functions of the applied voltage and actuator position. The actuator travel is 70 μm, limited by stops integrated into the flexure etch mask. The maximum lateral acceleration a_{max} is directly related to the maximum available force $F_{\max}$ of the actuator along the x-direction. The resonant frequency f_0 of the actuator is also related to $F_{\max}$ and is only measurable along the x-direction; motion in the out-of-plane direction (z axis) is strongly limited by squeeze-film damping and the resonant frequencies along the second lateral direction (y-axis) are much higher than the x-direction f_0 because of the design of

the folded beam flexures. Increasing the bias voltage increases the available force, but the bias voltage is constrained to be less than $V_{\rm snap}$, the bias voltage at which the translator snaps down onto the stator.

The lateral force F_x produced by the surface drive actuator is shown in Fig. 5(a) for an actuator held at a bias of 30 V. This actuator responds very differently than conventional comb-drives or voice coil actuators. A force is applied to the translator by shifting the voltage pattern rather than by increasing the bias voltage. Referring to Pattern A in Table I, the basically alternating voltage pattern is disrupted at electrodes 4 and 5. The position of the "disruption" is shifted by one electrode as Pattern A changes to Pattern B while the overall bias voltage remains constant at 30 V. This actuation method is analogous to that of a magnetic stepper motor. In fact, we use similar terminology to describe the behavior of our actuator. We say that the stator voltage has undergone a full "step" when the disruption has been shifted by one electrode. The voltage pattern can also be "microstepped"—shifted by less than a full electrode; e.g., Pattern D is shifted by 0.1 steps from Pattern C.

Each shift of the voltage pattern causes the translator to sit in a different potential well. As shown in Fig. 5(b), the force exerted on the translator depends not only on the voltage pattern applied to the stator, but also the position of the translator. Changing the voltage pattern by one step causes the force curve to shift by 400 nm and causes a translator initially positioned at the origin to experience a force of 95 μ_N to the right. The translator will accelerate to the right until it has moved 400 nm and has passed the zero force position of the new force curve. The force curve shown in Fig. 5(a) was determined by measuring the translator acceleration after the stator voltage pattern was changed. From the force curves it is evident that the acceleration decreases as the translator moves toward the zero crossing of a particular force curve and thus it is important to select a fairly short time over which to fit acceleration data. For the force data shown in Fig. 5(a), the translator position was fit over 85 μs, corresponding to 330 nm of motion when the voltage pattern is shifted by one step. This means that there were substantial changes in the applied force during the measurement; however the extended range was necessary to have good averaging of the capacitive sensor data.

Returning to Fig. 5(a), the lateral force increased linearly from zero with increasing number of steps in the voltage pattern—an effect corresponding to the translator lying in the roughly linear portion of the force curve. This linear relationship between applied force and electrode state facilitates the design of control electronics. When the voltage pattern was shifted more than three steps, the applied force in the x-direction saturated to F_{max}, implying that in this regime the initial position of the translator occurred at the upper part of the sinusoidal force curve. For voltage pattern changes greater than 4.5 steps, the available acceleration decreased approximately linearly with the number of steps. In this regime, the initial translator position occurred at the back of the force curve.

The relationship between actuator performance and applied bias is shown in more detail in Fig. 6. The measured resonant frequency and sensor output voltage both vary as functions of the applied bias. A simple mathematical model explains much

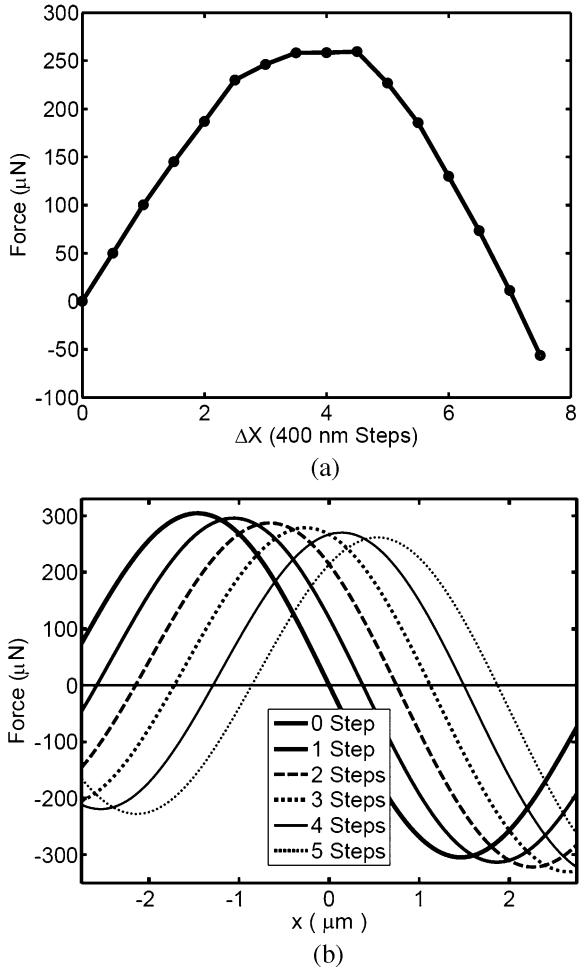

Fig. 5. (a) Acceleration produced by the actuator as a function of the shift, ΔX, in stator voltage profile. (b) Calculated actuator force as a function of the translator position. When the voltage profile is shifted by ΔX, the force profile shifts by the same amount and the translator experiences a force that depends on ΔX.

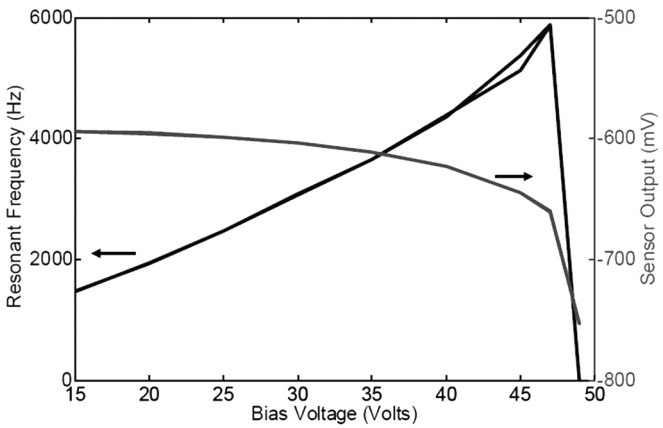

Fig. 6. Resonant frequency and sensor voltage at an arbitrary position w.r.t. applied bias voltage. The plot shows resonant frequency data as voltage is ramped up until it snaps down, and then as it is reduced. Snap in is observed at a bias voltage of 48 V, however, no hysteresis is observed due to it.

of the behavior of f_0. The x-direction resonant frequency f_0 of a surface drive actuator depends both on the mechanical spring constant k_m supplied by the bending of the silicon flexures and

on the electrical spring constant k_{es} supplied by the electrostatic potential

$$f_0 = \frac{1}{2\pi}\sqrt{\frac{1}{m}(k_m + k_{es})} = \frac{1}{2\pi}\sqrt{\frac{1}{m}\left(k_m + \frac{\pi}{p_t}F_{\max}\right)} \quad (4)$$

and

$$F_{\max} = \frac{\varepsilon_0 k^2 V_b^2 J_s J_t}{2\sinh(kd)} \text{ from equation (1) and Fig. 4.} \quad (5)$$

There are three distinct regions in Fig. 6 and each section is important in verifying and characterizing the mechanical and electrical behavior of the actuator. The first region occurs at moderate bias voltage (10–35 V) where $k_{es} \gg k_m$ and the resonant frequency is linear in V_b. This behavior is expected from (4) and (5) as long as any variations in the gap d are small compared to the gap itself. From the data in this voltage range, we find that $f_0 \sim V_b \times (110\ \mathrm{Hz/V})$. The stage mass m is simple to calculate since it is a 2-D shape projected through a 100 μm thick SOI layer; $m = 1.09$ mg. Since the force curve shown in Fig. 2(b) is nearly purely sinusoidal, the f_0 data implies that $F_{\max} \sim (0.466\ \mu\mathrm{N/V}^2)V_b^2$. Using this value of F_{max} and the designed electrode area of 1.84 mm^2, (5) predicts a translator-stator gap d of 2.6 μm—close to the design gap of 2.5 μm. These same data and the number of steps the actuator moves before the spring force is greater than F_{max} determine that k_m from the flexures is 16 N/m.

At higher V_b, the translator gap d is no longer relatively constant. In this second region ($V_b \sim 35\ \mathrm{V} - 45\ \mathrm{V}$), the out-of-plane force V_z expressed in (2) becomes large enough to significantly deform the high aspect ratio flexures. Similar to a gap closing actuator, the actuator gap decreases with increasing V_b and this in turn causes f_0 to increase supralinearly with V_b. The sensor output voltage also exhibits a significant voltage dependence in this region, indicative of the changing gap. Data in this region can be used to determine the out-of-plane stiffness of the flexures supporting the translator. We find $k_z \sim 2700\ \mathrm{N/m}$ and $k_z/k_m \sim 170$. This is somewhat smaller than we would expect from a finite element model of the flexures, but still demonstrates a significant out-of-plane to in-plane stiffness ratio.

In the third region of Fig. 6, V_b is greater than 48 V and the translator snaps down to the stator. At snap in, the translator hits the bumpers and the translator becomes overdamped with no observed resonant frequency. The sensor output also shows a sudden change in sensor output, exhibiting a sudden increase in sensitivity as the translator snaps down. The data shown in this figure was taken when first increasing and then decreasing the bias voltage. The data while ramping down almost fully traces back the ramp up data, showing no hysteresis and no irrecoverable damage due to snap in. This snap-in voltage agrees well with a 47.2 V snap-in voltage calculated from (2) and (3) using the designed electrode area of 1.84 mm^2 and the experimentally determined initial gap of 2.6 μm and $k_z = 2700\ \mathrm{N/m}$.

Accurate modeling of the electrostatics is also critical to understand the relationship between actuator position and resonant frequency f_0 shown in Fig. 7. Fig. 7(a) shows the effect of the folded beam flexures on f_0. As the actuator moves away from the relaxed position of the flexures along the x-direction, the electrostatic potential must counteract the increasing restoring

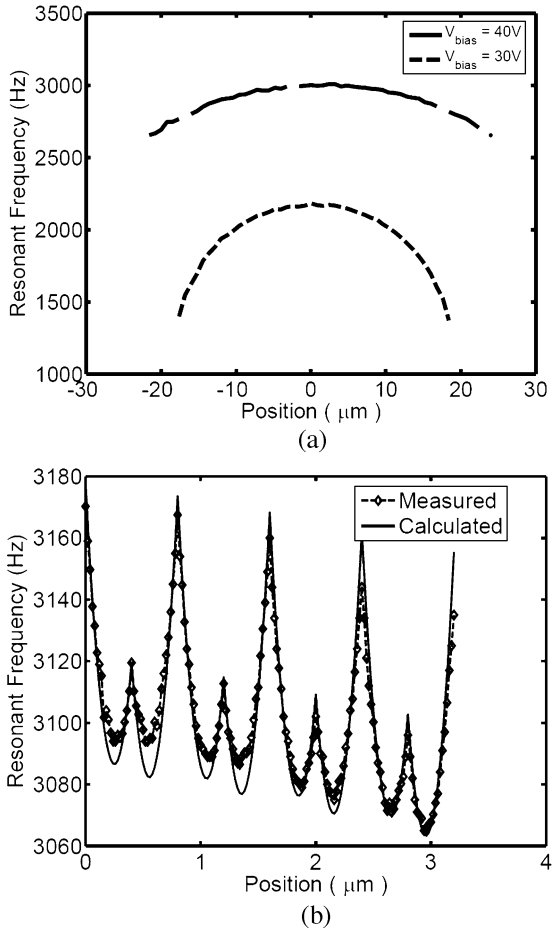

Fig. 7. (a) Resonant frequency variation with large changes in position. (b) Resonant frequency variation with microstepping at $\mathrm{V_{bias}} = 30\ \mathrm{V}$. The parameters used for the calculated curve are $\mathrm{V_b} = 30\ \mathrm{V}$, gap $= 2.4\ \mu\mathrm{m}$, $\mathrm{k_t} = 10\ \mathrm{N/m}$, and $\mathrm{k_z} = 3500\ \mathrm{N/m}$.

force of the flexures. As the actuator rides up the sinusoidal force curve, the electrostatic contribution to f_0 diminishes. At $V_b = 30$ V, the electrostatic force curve is relatively shallow so f_0 is strongly dependent on motor position and the flexural restoring force limits the travel to 17 μm in either direction. At $V_b = 40$ V, the electrostatic force curve is larger and the resonant frequency is less dependent on actuator position.

More complex behavior is visible in Fig. 7(b). The translator x position was varied in microsteps of 40 nm by incrementing the electrode voltage in steps of one tenth of V_b. The intricate 2.5% scalloping of the resonant frequency arises from the fact that the magnitudes of the Fourier transform components J_t and J_s in (1)–(4) are somewhat dependent on the voltage pattern. Similar torque ripple is seen for magnetic stepper motors [28]; however the ripple has the reverse sign and is four times greater for the same number of poles.

An interesting effect is evident in Fig. 7(b) that is not seen with magnetic motors—f_0 measured at even steps is 1.5% larger than that measured at odd numbered steps. The f_0 difference arises from the translator surface potential being significantly less than 0.5 V_b. In the even states, four stator electrodes are held at V_b and three stator electrodes are held at ground; thus the average stator potential is greater than 0.5 V_b. The mismatch in the average potentials pulls the translator toward the stator,

decreasing the gap d in (1), and increasing f_0. Conversely, in odd states, the average potentials of the two surfaces are more nearly equal and f_0 is reduced. Finite element models of the translator predict similar behavior because the potential on the translator surface "sees" the grounded body of the translator through the thin (0.17 μm) dielectric on the translator. The calculated curve in Fig. 7(b) captures most of the behavior of the resonant frequency with only one fitting parameter—the amount that the translator substrate is "seen" through the insulator. The gap and spring constants of the flexures were determined by the frequency versus voltage and travel versus voltage data.

VI. Operation in Air

For many applications, operation in air is an essential requirement. Unfortunately, our previously reported surface drive actuators had significant problems operating in air [23], [27]. The earliest actuators used exposed Cr as the electrode material and upon the application of a bias voltage greater than ~10 V, water would condense from the atmosphere and dissolve the Cr electrodes. Later versions of the actuator used polysilicon electrodes. These electrodes were more stable but would eventually break down, presumably because of shorting from adsorbed layers.

The passivated electrodes used in the current motor (Fig. 3) do not exhibit any of these failure mechanisms; however, as shown in Fig. 8, the performance of *as fabricated* motors degrades substantially with time when exposed to air. The 60% drop in f_0 implies that only 16% of the original force is available after ten minutes in air. To determine the source of the performance degradation, the voltages on all electrodes were "flipped" at 10 min intervals—that is, electrodes whose voltages initially held at ground were switched to V_b and *visa versa*. The decay that occurs during the 10 min interval is fully recovered after "flipping" the voltages—indeed, f_0 immediately after the "flip" is even larger than the initial *as fabricated* f_0. This indicates that the performance degradation is caused by mobile charges that shield the voltages on the electrodes except immediately after the "flip" when these mobile charges add to the voltage applied to the electrodes.

A variety of methods were used to mitigate the shielding effects seen in the *as fabricated* data of Fig. 8. The shielding is apparently mediated by water vapor since f_0 is stable in a nitrogen environment. However, hydrophobic coatings, both plasma deposited CF_x and vapor deposited tridecafluoro-1,1,2,2-tetrahydrooctyltrichlorosilane (FOTS), had very little effect on the shielding. Fortunately, a simple anneal of the *as fabricated* motors in vacuum or standard atmosphere eliminated the f_0 decay. As shown in Fig. 8, the f_0 decay after baking has a decay constant on the order of days rather than seconds. It is not clear how the anneal stabilizes the surface since X-ray photoemission spectroscopy (XPS) did not show any change in the organics present on either the translator or stator surfaces. With this long decay constant, excellent actuator performance can be achieved by flipping the voltages occasionally.

VII. Discussion

Selecting an actuator for a particular application is a complex process involving the consideration of a variety of performance features such as force, travel, size, efficiency, cost, speed, reliability, resonant frequency, voltage, power, temperature, and environmental constraints among others. A detailed discussion

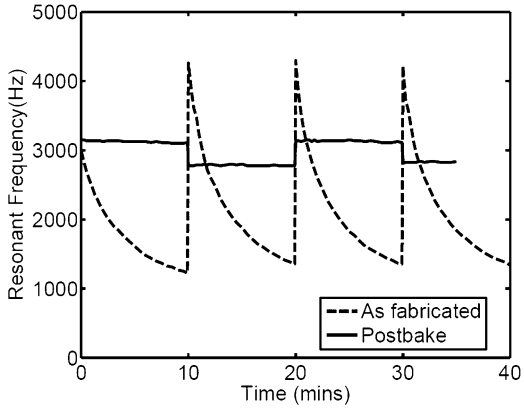

Fig. 8. Resonant frequency variation with time during air operation at $V_{bias} = 40$ V. The dashed curve shows the considerable decay of resonant frequency evident in devices before post-bake. The solid curve shows negligible decay in air for the same device after a 2.5 h vacuum bake. At every 10 min interval, the polarity of the voltages on all translator and stator electrodes was flipped.

of the appropriate evaluation methods cannot be done justice in this paper and a good overview is provided elsewhere [29]. We have found a simple metric to determine whether a given actuator should even be considered for a particular application. In this method, the specific work (Force × Travel/Area) generated by an actuator is compared to the requisite force and travel, the two most accessible requirements of a particular application. Thus, this metric is the first hurdle that an actuator must satisfy before being considered for an application.

We have found that the specific work is a particularly difficult hurdle for micromachined actuators to pass. In Fig. 9, the specific work is plotted for several micromachined actuators and conventional milliactuators. Though certainly not exhaustive, we believe this plot is representative of present state-of-the-art actuators. Surprisingly, the micromachined actuators are fairly tightly clustered below 10 μN/mm, with the comb drive actuator from ioλon achieving slightly greater than 10 μN/mm [22]. It is interesting that micromachined actuators employing such wide varieties of actuation mechanism—thermal [30], electrostatic [10], and magnetic [31]—achieve very similar specific work. A factor of ten separates the micromachined actuators from the conventional milliactuators, which are generally permanent magnet devices. These actuators are key elements in many popular consumer products from watches [32] to CD players to the ubiquitous relay (NOTE: For a TQ2-5 V relay produced by Aromat [33], a subsidiary of Matsushita Corporation, the authors measured an average force of 60 mN over 300 μm travel. The actuator dimensions were $14 \times 9 \times 5$ mm^3). Piezoelectric devices provide still larger specific work, examples are the Physic Instruments PI243.11 [34] and the NEC Tokin AE0203D04 [35].

Several important choices are made in constructing this metric. First, available work is chosen rather than available power because of the difficulty in producing a reliable micro-scale transmission. Second, the available work is scaled to the area of the actuator rather than the volume or mass. For micromachined actuators, area is the obvious scaling factor because the available work usually depends linearly on the actuator area. For milliactuators, the available work varies

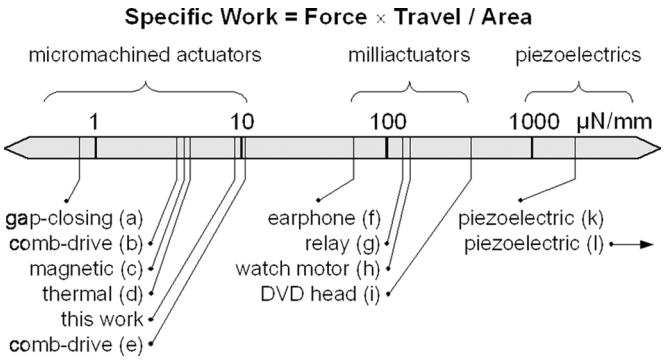

Fig. 9. Specific work plotted for various actuators. (a) Lucent micromirror, an estimate. (b) Sandia comb-drive [10]. (c) IBM millipede [6], (d) thermal bimorph [30]. (e) I/O λ on comb drive [22]. (f) Conventional earphone actuator, an estimate. (g) Aromat TQ2-5 V relay, see related note in text. (h) Watch motor [32]. (i) DVD head, an estimate. (k) Physik instrumente piezoelectric actuator 841.11. (l) NEC tokin AE0203D04 stacked piezoelectric actuator.

as $(\text{Area})^n$ where n is between 1.5 and 2.5 [36], [37], but for many applications, such as relays or watch motors, the important size constraint is the two largest dimensions rather than the overall volume or mass. This plot should only be used to evaluate applications for which frictional actuators would not be appropriate because travel is not well defined for such actuators [12], [38]–[40].

From this very simple comparison, we conclude that micromachined actuators still require an order of magnitude increase in their specific work before they are likely to be used for applications that prove ubiquitous. This order of magnitude increase is likely achievable with increased process control for the present MEMS actuators. By reducing the gap and electrode line-widths of the surface drive motors described in this paper, a specific work similar to that of milliactuators should be achievable.

VIII. Conclusion

In this paper, we have been able to demonstrate an actuator with large travel length, large acceleration and capability to operate in air. Most significant variations and behaviors have been understood and explained from basic physics of the device. We believe that the surface actuators described in this paper provide a path to positioning real world objects.

Acknowledgment

The authors would like to thank Y.-L. Chang for XPS characterization of the stator and translator surfaces; D. Sulchek and K. Seaward for the deposition of hydrophobic coatings; and M. Shipley and R. Verghese for process development at Agilent, Fort Collins, CO.

References

[1] Small and Thin ±5 g Accelerometer Analog Devices Inc.. Norwood, MA, ADXL320 datasheet, Rev. 0, p. 12, Sep. 2004.

[2] L. J. Hornbeck, "Digital light processing and MEMS: An overview," Advanced Applications of Lasers in Materials Processing/Broadband Optical Networks/Smart Pixels/Optical MEMs and Their Applications/ IEEE LEOS Summer Topical Meetings pp. 7–8, 1996.

[3] J. D. Berger, Y. Zhang, J. D. Grade, H. Lee, S. Hrinya, and H. Jerman, "Widely tunable external cavity diode laser based on a MEMS electrostatic rotary actuator," in *Proc. Optical Fiber Communication Conf.*, Anaheim, CA, 2001, pp. TuJ1–TuJ4.

[4] J.-J. Choi, H. Park, K. Y. Kim, and J. U. Jeon, "Electromagnetic micro x-y stage with very thick Cu coil for probe-based mass data storage device," *J. Semiconductor Technol. Sci.*, vol. 1, p. 84, 2001.

[5] H. Rothuizen, U. Drechsler, G. Genolet, W. Häberle, M. Lutwyche, R. Stutz, R. Widmer, and P. Vettiger, "Fabrication of a micromachined magnetic x/y/z scanner for parallel scanning probe applications," *Microelect. Eng.*, vol. 53, pp. 509–512, 2000.

[6] P. Vettiger, G. Cross, M. Despont, U. Drechsler, U. Dürig, B. Gotsmann, W. Häberle, M. A. Lantz, H. E. Rothuizen, R. Stuitz, and G. K. Binnig, "The "Millipede"—nanotechnology entering data storage," *IEEE Trans. Nanotechnol.*, vol. 1, no. 1, pp. 39–55, Jan. 2002.

[7] J. D. Grade, H. Jerman, and T. W. Kenny, "A large-deflection electrostatic actuator for optical switching applications," in *Proc. Solid-State Sensor and Actuator Workshop*, Hilton Head, S.C., 2000, pp. 97–100.

[8] S. Hoen, Optical Cross-Connect Switch Using Dual-Axis Micromirror Arrays 1999, HP Docket No. 10991566.

[9] S. L. Miller, P. J. McWhorter, M. S. Rodgers, J. L. Sniegowski, and S. M. Banes, "Microelectromechanical apparatus for elevating and tilting a platform," World Intellectual Property Organization Sandia Corporation. Albuquerque, NM, 2001.

[10] M. S. Rodgers, S. Kota, J. Hetrick, Z. Li, B. Jensen, T. W. Krygowski, S. L. Miller, S. M. Barnes, and M. S. Burg, "A new class of high force, low-voltage, compliant actuation systems," in *Proc. Solid-State Sensor and Actuator Workshop*, Hilton Head, SC, 2000, pp. 210–213.

[11] V. Aksyuk, B. Barber, C. R. Giles, R. Ruel, L. Stulz, and D. Bishop, "Low insertion loss packaged and fibre connectorised MEMS reflective optical switch," *Electron. Lett.*, vol. 34, pp. 1413–1414, 1998.

[12] D. L. Luck, M. P. de Boer, W. R. Ashurst, and M. S. Baker, "Evidence for pre-sliding tangential deflections in MEMS friction," in *Proc. Solid-State Sensors, Actuators and Microsystems*, Boston, MA, 2003, pp. 404–407.

[13] R. Legtenberg, E. Berenschot, M. Elwenspoek, and J. Fluitman, "Electrostatic curved electrode actuators," in *Proc. IEEE Micro Electromechanical Systems Workshop*, Amsterdam, The Netherlands, 1995, pp. 37–42.

[14] T. D. Kudrle, G. M. Shedd, C. C. Wang, J. C. Hsiao, M. G. Bancu, G. A. Kirkos, N. Yazdi, M. Waelti, H. Sane, and C. H. Mastrangelo, "Pull-in suppression and torque magnification in parallel plate electrostatic actuators with side electrodes," in *Proc. Solid-State Sensors, Actuators and Microsystems*, Boston, MA, 2003, pp. 360–363.

[15] D. P. Arnold, F. Cros, I. Zana, M. G. Allen, S. Das, and J. H. Lang, "Magnetic induction machines embedded in fusion-bonded silicon," in *Proc. Int. Conf. on Solid-State Sensors and Actuators*, Hilton Head Island, SC, 2004, pp. 120–123.

[16] H. Guckel, K. Fischer, and E. Stiers, "Closed loop controlled, large throw, magnetic linear microactuator," in *Proc. 11th Annu. Int. Workshop on Microelectromechanical Systems*, 1998, pp. 414–418.

[17] H. Guckel, T. R. Christenson, K. J. Skrobis, T. S. Jung, J. Klein, K. V. Hartojo, and I. Widjaja, "A first functional current excited planar rotational magnetic," in *Proc. Investigation of Micro Structures, Sensors, Actuators, Machines, and Systems*, 1993, pp. 7–11.

[18] Y. Lu and C.-J. Kim, "Micro-finger articulation by pneumatic parylene balloons," in *Proc. Solid-State Sensors, Actuators and Microsystems*, Boston, MA, 2003, pp. 276–279.

[19] W. L. Benard, H. Kahn, A. H. Heuer, and M. A. Huff, "A titanium-nickel shape-memory alloy actuated micropump," in *Proc. Solid State Sensors Actuators*, Chicago, IL, 1997, pp. 361–364.

[20] T. Namazu, S. Inoue, Y. Tashiro, Y. Okamura, and K. Koterazawa, Ti-Ni SMA Film Actuated Si Cantilever Beams for MEMS Probe Card 2005, vol. 1, p. 736.

[21] J. D. Grade and H. Jerman, "MEMS electrostatic actuators for optical switching applications," in *Proc. Optical Fiber Communication Conf. Exhibit*, 2001, vol. 3, pp. 361–364.

[22] J. D. Grade, H. Jerman, and T. W. Kenny, "Design of large deflection electrostatic actuators," *J. Microelectromech. Syst.*, vol. 12, no. 3, pp. 335–343, Jun. 2003.

[23] S. Hoen, Q. Bai, J. A. Harley, D. A. Horsley, F. Matta, T. Verhoeven, J. Williams, and K. R. Williams, "A high-performance dipole surface drive for large travel and force," in *Proc. Solid-State Sensors, Actuators and Microsystems*, Boston, MA, 2003, pp. 344–347.

[24] S. Hoen and C. Taussig, "Electrostatic actuator with alternating voltage patterns," U.S. U.S. Patent 5,986,381, 1999.
[25] P. A. Stupar, R. L. Borwick, III, and J. DeNatale, "Liquid packaging for MEMS sensors and RF devices," in *Proc. Solid-State Sensors, Actuators and Microsystems*, Boston, MA, 2003, pp. 1836–1839.
[26] P. G. Hartwell, R. G. Walmsley, D. J. Fasen, and S. T. Hoen, "Integrated position sensing for control of XY actuator," in *Proc. Sensors*, Vienna, Austria, 2004, pp. 1407–1410.
[27] S. Hoen, P. Merchant, G. Koke, and J. Williams, "Electrostatic surface drives: Theoretical considerations and fabrication," in *Proc. Int. Conf. Solid-State Sensors and Actuators*, Chicago, IL, 1997, pp. 41–44.
[28] L. K. Baxter, *Capacitive Sensors: Design and Applications*. New York: IEEE Press, 1997.
[29] A. H. Slocum, *Precision Machine Design*. Dearborn, MI: So. Manufact. Eng., 1992.
[30] J. H. Comtois and V. M. Bright, "Applications for surface-micromachined polysilicon thermal actuators and arrays," *Sensors Actuators*, vol. A 58, pp. 19–25, 1997.
[31] H. Rothuizen, M. Despont, U. Drechsler, G. Genolet, W. Häberle, M. Lutwyche, R. Stutz, and P. Vettiger, "Compact copper/epoxy-based electromagnetic scanner for scanning probe applications," in *Proc. IEEE 15th Int. Conf. Microelectromechanical Systems*, Las Vegas, NV, 2002, pp. 582–585.
[32] R. Grandjean, "Moteur biphase pour montre a quartz," in *Proc. 57th Congr. Societe Suisse de Chronometrie*, Montreux, Switzerland, 1982, pp. 147–151.
[33] TQ2-5 V Relay, Product Datasheet Panasonic. Osaka, Japan.
[34] AE0203D04 Piezoelectric Actuator, Product lit. NEC Tokin. Tokyo, Japan, 2006.
[35] Physik Instrumente Product Datasheet. Karlsruhe/Palmbach, Germany, 2005, PI243.11.
[36] J. H. Marden and L. R. Allen, "Molecules, muscles, and machines: universal performance characteristics of motors," in *Proc. Natl. Acad. Sci.*, 2002, vol. 99, pp. 4161–4166.
[37] W. S. N. Trimmer, "Microrobots and micromechanical systems," *Sensors Actuators*, vol. 19, pp. 267–287, 1989.
[38] P-915K094 Miniature Rotary PiezoMotor, Product Data Sheet Physik Instrumente. Karlsruhe/Palmbach, Germany.
[39] J. Frohn, J. F. Wolf, K. Besocke, and M. Teske, "Coarse tip distance adjustment and positioner for a scanning tunneling microscope," *Rev. Sci. Instrum.*, vol. 60, pp. 1200–1201, 1989.
[40] R. Yeh, S. Hollar, and K. S. J. Pister, "Single mask, large force, and large displacement electrostatic linear inchworm motors," *J. Microelectromech. Syst.*, vol. 11, pp. 330–336, 2002.

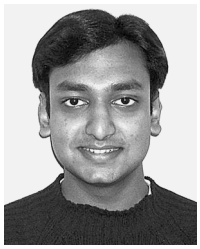

Manu Agarwal (S'01–M'06) received the B.Tech. degree in electrical engineering from the Indian Institute of Technology, Kanpur, in 2003, and the M.S. degree in electrical engineering from Stanford University, Stanford, CA, in 2005. He is currently working toward a Ph.D. degree in electrical engineering at Stanford University.

During his undergraduate career, he interned at the Technical University of Ilmenau, Ilmenau, Germany, and at the Ecole Polytechnique Fédérale de Lausanne (EPFL), Switzerland. During his graduate career, he interned at Agilent Labs, Palo Alto, CA, where he worked on characterizing dipole surface drive MEMS actuators. His current research interests include design of high frequency MEMS resonators for frequency references, specifically in characterization of the nonlinearities and on studying phase noise in electrostatic MEMS resonators.

David T. Dutton received the B.S. (Hons) degree in electrical engineering from the University of Kent, Canterbury, U.K., in 1990.

He has worked in defense and commercial electronics covering materials characterization and semiconductor device processing of both III-V and II-VI semiconductors, with GEC Marconi IR Ltd, DERA-Defence Evaluation Research Agency, Malvern, U.K. (now Qinetiq), and Agilent Technologies, Ipswich, U.K. He began research at Agilent Labs, Pallo Alto, CA, in 2001, concentrating on device processing of III-V devices and Si micromachines and has since moved onto investigations into microplasma applications.

Jeremy A. Theil (M'88–SM'01) received the B.S. degree in metallurgical engineering and materials science from Carnegie Mellon University, Pittsburgh, PA, in 1985, the M.S. degree in materials science and engineering from the University of Illinois, Urbana-Champaign, in 1988, and the Ph.D. degree in materials science and engineering from North Carolina State University, Raleigh, in 1992.

He was with the Central Research Laboratory of Johnson Controls, Glendale, WI, from 1992 until 1995, when he joined HP Laboratories, Palo Alto, CA, of the Hewlett-Packard Company. He joined Hewlett-Packard's spin-off Agilent Technologies, Santa Clara, CA, in 1999, and stayed until 2005 when he joined Lumileds Lighting, San Jose, CA (now Philips Lumileds Lighting). At HP Laboratories, he pioneered the development of high quality a-Si:H p-i-n photodiodes for silicon CMOS image sensors. His interests include development of novel transducers and actuators that can be monolithically integrated into Si, and the development of high power light-emitting diodes.

Dr. Theil is also a member of the Materials Research Society (MRS), and the American Vacuum Society. He is an inventor of over 44 patents, has authored 33 papers, and chaired the 2005 MRS Symposium on Monolithic Instruments.

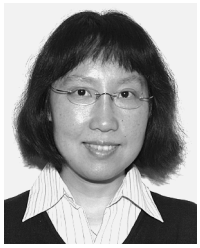

Qing Bai received the B.S. degree in electrical engineering from Zhejiang University, Hangzhou, China, in 1990, and the M.S. and Ph.D. degrees in electrical engineering from the University of Michigan, Ann Arbor, in 1994 and 1999, respectively.

She currently works at Agilent Technologies, Inc., Santa Clara, CA, on nano measurement instrument. Her research interests are in MEMS devices, IC design, and nano measurement systems.

Evelyn Par, photograph and biography not available at the time of publication.

Storrs Hoen (M'00) received the B.E. degree in materials engineering, electrical engineering, physics, and mathematics from Vanderbilt University, Nashville, TN, in 1984, the M.A. degree in physics and philosophy from Oxford University, Oxford, U.K., in 1986, and the Ph.D. degree in condensed matter physics from the University of California, Berkeley, in 1992.

He worked at IBM Almaden Research Center, San Jose, CA, in advanced data storage from 1992 to 1994, and joined Hewlett-Packard Laboratories, Palo Alto, CA, in 1994. At HP and its successor, Agilent Technologies, he has invented and developed MEMS actuators for atomic resolution data storage and optical telecommunications and has invented valving solutions for printheads. He is the author of 37 patents and over 20 publications.